Supplementary material

Efficient Catalytic Light-Driven Micromotors Enable Low-Magnification Tracking under Photoluminescence and Applications in Complex Media

*Xinwen Gao, Yuyang Zhang, Wenyang Huang, Yuhan He, and Tingting Yu**

This PDF file includes:

Figures S1 to S9

Notes S1 to S7

Tables S1 to S3

Legends for movies S1 to S14

Other Supplementary material for this manuscript includes the following:

Movies S1 to S14

Table S1. Classification and Characteristics of Fluorescent Materials Commonly Used in Micro-Nano Fields.

Forms of Bismuth Vanadate	Categorized by Application	Practical Applications	Advantages	Ref
(Cu–Bi/$BiVO_4$) microplates	Photocatalyst	photocatalytic CO_2 reduction into valuable chemical fuels.	Increased photocatalytic CO_2 conversion efficiency was obtained.	1
Snow-like $BiVO_4$		degradation of ciprofloxacin	stronger ability of producing reactive oxygen species (ROSs)	2
$CuO/BiVO_4$		Efficient Production of Aromatic Chemicals	Significantly suppresses electron-hole recombination and extends carrier lifetime	3
$BiVO_4$ Nanoflakes		Photocatalyst	Outstanding photocatalytic OER performance	4
m- $BiVO_4$ nanoribbons		High-efficiency photocatalytic reactions of MB	A material with a large specific surface area and enhanced photocatalytic activity, as well as reusability and chemical stability.	5
Nanoporous $BiVO_4$ Photoanodes	Photoanode	Photocathode	High electron-hole separation efficiency optimizes both the $BiVO_4$/OEC and the OEC/electrolyte junctions simultaneously.	6
$BiVO_4/TiO_2$–N nanotubes		Photoanode	The UV–visible light absorption ability is broadened.	7
OV-$BiVO_4$/TA-Co photoanode		photoanode candidate	The photoelectrochemical (PEC) water splitting performance of the photocathode has been significantly improved.	8
Nanoscale-thick film Ce–$BiVO_4$		Photoanode	A First Analysis of the Effects of Cerium on the Physical Properties and PEC Semiconductor Performance During Water Splitting	9
$BiVO_4$/ITO		PEC sensor	Its excellent stability makes it sensitive, robust, and readily available.	10
Co-Bi+ $BiVO_4$		Photoanode	Improving the performance of photoanodes in terms of photogenerated current	11
CQDs- $BiVO_4$		Solar Power Converter	Improved PEC performance	12

Star-shaped $BiVO_4$ micromotors		Transportation, disinfection	Light initiates collective self-assembly and disassembly, but it does not produce photoluminescence, and H_2O_2 is needed to speed up the process.	[13]
CNP/B-$BiVO_4$/WO_3	Micromotor	Dirt removal	Exhibits strong responsiveness to visible light and effective charge separation but necessitates dopants.	[14]
Hexagon-$BiVO_4$		**Low-magnification tracking and environmental cleanup.**	**High-efficiency multi-band control, robust autofluorescence for population-level tracking, and exceptional environmental adaptability**	**This work**

Supplementary Note 1: A Comparative Review of Current Research on Bismuth Vanadate Materials

To better define the scope of this work, we systematically reviewed numerous representative studies on $BiVO_4$ and compiled a list of research articles focusing on various morphologies and applications of bismuth vanadate, as shown in **Table S1**. As can be seen, bismuth vanadate exhibits a wide variety of morphologies, encompassing microsheets, nanoribbons, nanotubes, thin films, star-shaped micromotors, and other microstructures. By modifying the morphologies of bismuth vanadate and introducing various dopants, researchers have further analyzed how the crystalline state of bismuth vanadate varies under different preparation conditions and how to enhance its photocatalytic performance. [15, 16] At the same time, most current research focuses on improving the electrolytic performance of $BiVO_4$-based photoelectrodes and optimizing the intrinsic photocatalytic performance of the material. Application scenarios are highly concentrated on PEC electrodes and photocatalysts. The core problem addressed by these studies is "how to make $BiVO_4$ generate electricity or degrade pollutants more efficiently," but few directly translate these light-responsive properties into "mobile micro- and nano-devices." Publications on bismuth vanadate-based micromotors are scarce, and existing approaches each have their limitations: some require external fuel to move rapidly in pure water, [17] while others have a narrow range of light-driven response. Furthermore, although the fluorescence of bismuth vanadate has long been reported, there have been no reports of its application in micromotors. Some studies have utilized lanthanide doping to achieve luminescence in bismuth vanadate micromotors [18] or loaded gold nanostars to enable surface-enhanced Raman spectroscopy (SERS) in situ detection; [19] however, neither approach offers the advantages of the intrinsic luminescence of bismuth vanadate micromotors.

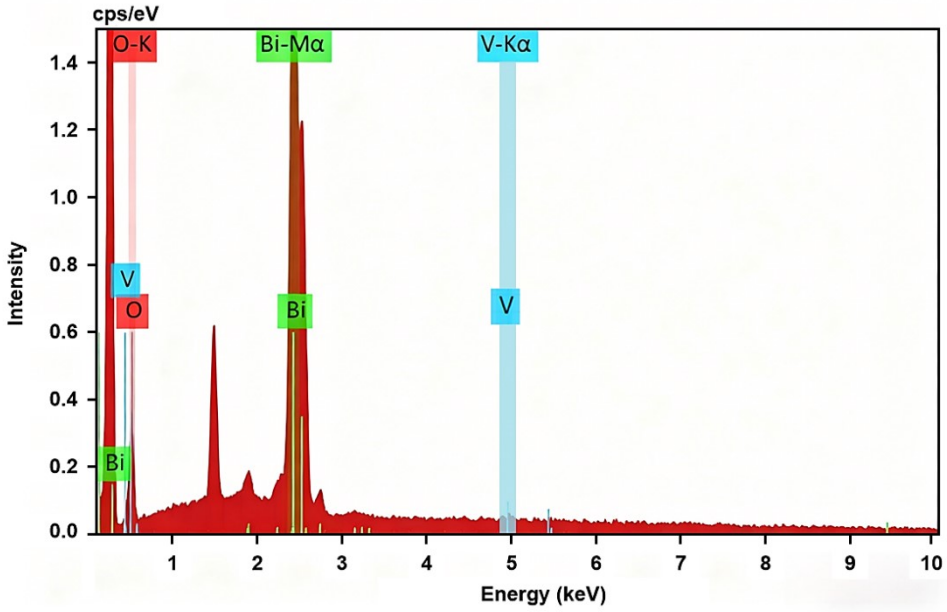

Figure S1. Energy-dispersive X-ray spectroscopy (EDS) spectrum of the Hexagon-$BiVO_4$ micromotors sample.

Figure S1 shows an energy-dispersive X-ray spectroscopy (EDS) spectrum of the sample, depicting its elemental composition. The x-axis shows energy (keV), while the y-axis denotes count rate (cps eV^{-1}). The height and area of the EDS peaks indicate the relative elemental content (semi-quantitative analysis).

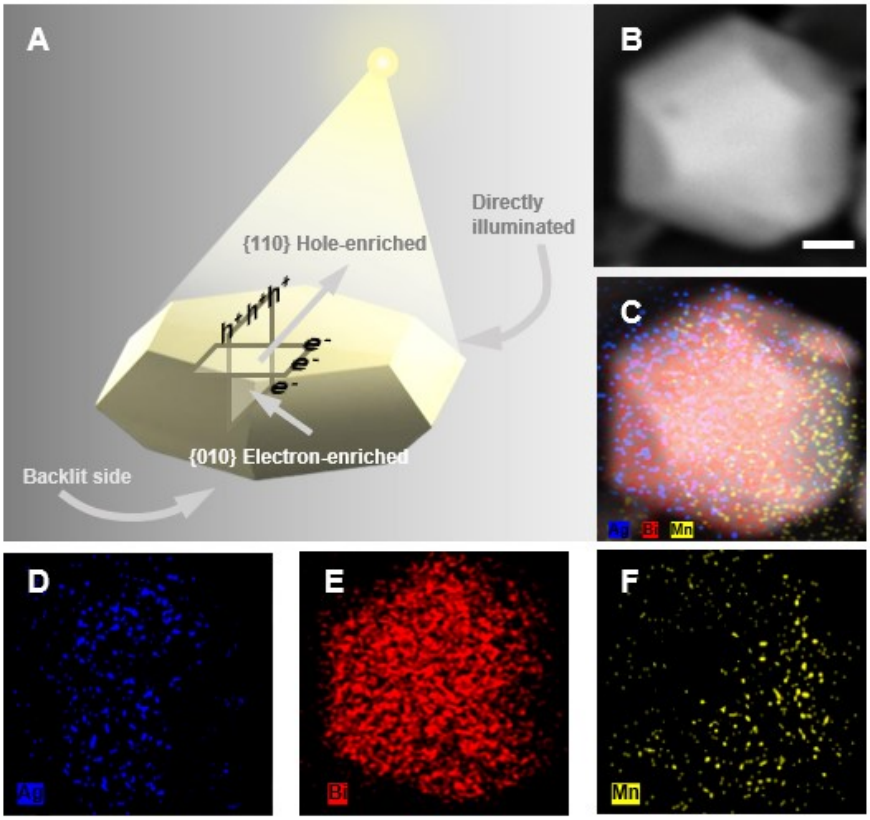

Figure S2. Asymmetric photoelectrochemical response of Hexagon-$BiVO_4$ arising from crystal structure and illumination geometry. (A) Asymmetric illumination geometry of the micromotor. **(B)** SEM image of Hexagon-$BiVO_4$ following selective deposition. Scale bars, 1 μm. **(C)** EDS elemental overlay showing Ag, Bi, and Mn distributions. **(D-F)** EDS-mapping of Ag, Mn, and Bi after selective deposition.

Supplementary Note 2: Crystal plane asymmetry

The Hexagon-$BiVO_4$ micromotors discussed in this work are not perfectly symmetric. As shown in **Figure S2A**, only the side directly exposed to light receives illumination, leaving the rear side without effective light exposure and resulting in uneven photoelectrochemical responses between the top and bottom. In the $BiVO_4$ crystal, photogenerated electrons tend to gather on the {010} facets, while holes accumulate on the {110} facets, indicating an asymmetry caused by the crystal structure. To confirm this asymmetric reaction, we conducted a metal-selective deposition experiment: we added the reducing agent Ag+ and the oxidizing agents Mn^{2+} and $K_2S_2O_3$ into an aqueous solution with the micromotor, stirred vigorously at room temperature, then washed and dried the sample after 5 hours of UV light exposure. [20] EDS analysis (**Figure S2C-F**) showed that Ag and Mn deposition sites did not completely overlap, indicating a crystal-induced electron-hole asymmetry during micromotor reactions. Further SEM-EDS analysis on multiple micromotors post-reaction confirmed that asymmetric oxidation-reduction reactions take place. To measure this asymmetry, we introduced an elemental distribution asymmetry coefficient, δ. The hexagonal structure was split into two symmetrical parts by a line connecting opposite vertices, skipping two vertices in between. Using ImageJ software, the average EDS signal intensity for each element was measured separately in each region. The elemental distribution asymmetry coefficient δ was calculated as $\delta = |T_1 - T_2| / (T_1 + T_2)$, where T_1 and T_2 represent the total EDS signal intensities of the same element on the two sides of the symmetry axis. The value of δ ranges from 0 to 1, where values closer to 0 signify a more symmetric elemental distribution. A threshold of 0.1 was established; if $\delta \leq 0.1$, the element is considered to be symmetrically distributed along the symmetry axis. If $\delta > 0.1$, the element distribution shows a measurable asymmetry. The micromotor in **Figure S2** has a δ of 0.31, and all other samples examined had

δ values greater than 0.1. These measurements confirm that the asymmetric distribution of electrons and holes caused by the crystal persists during the micromotor reaction.

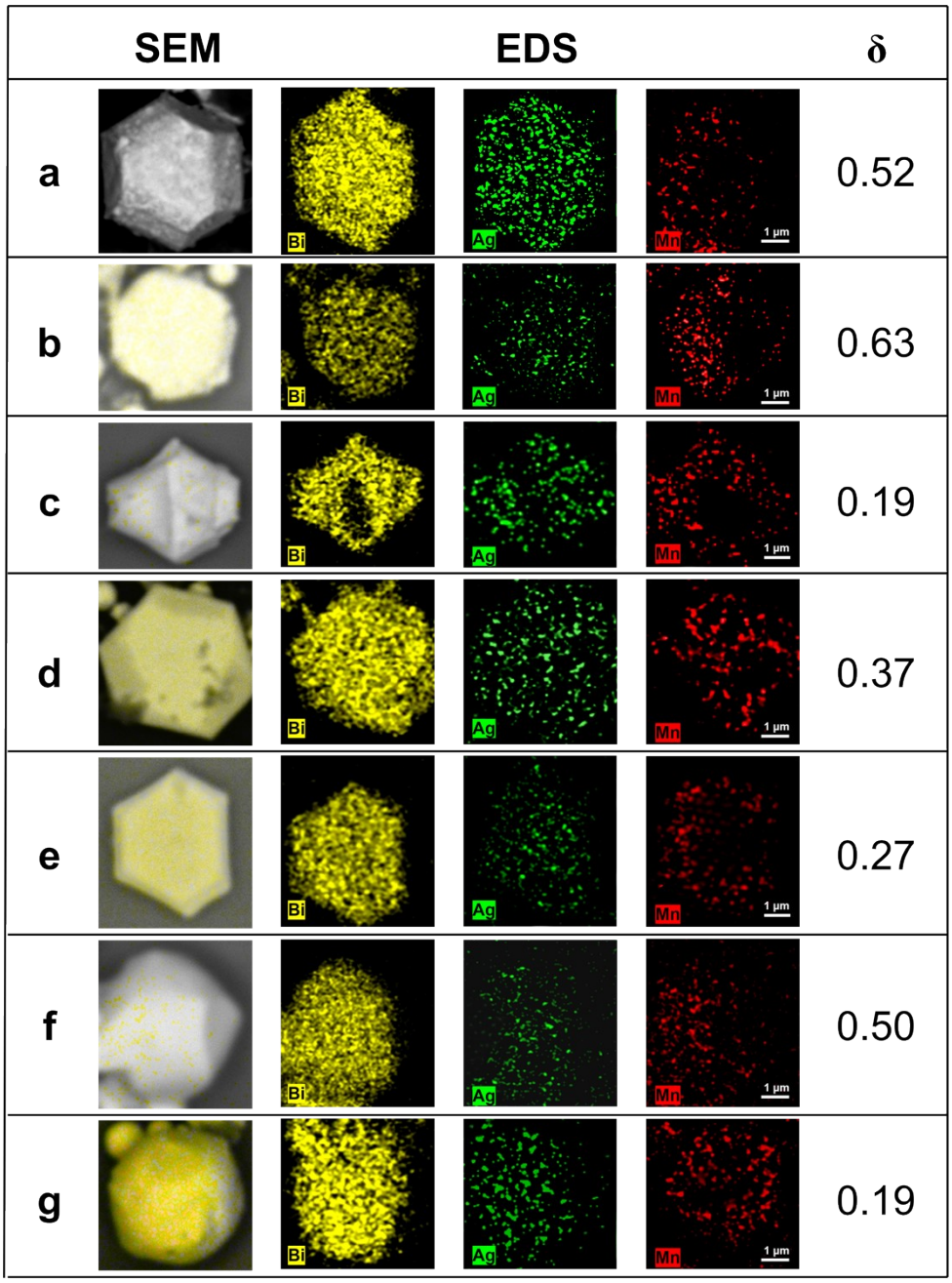

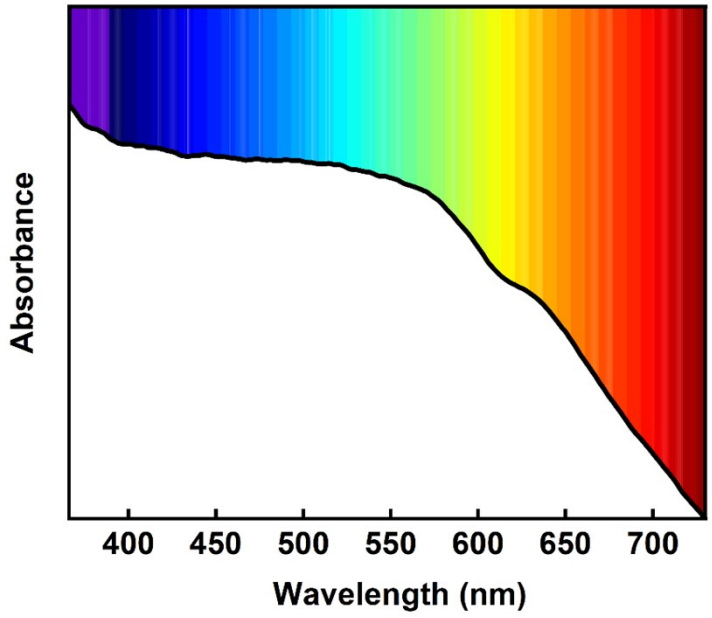

Figure S3. Absorption spectrum of Hexagon-$BiVO_4$ micromotors.

The material exhibits strong absorption at short wavelengths (ultraviolet and blue light), with a notable decrease in absorbance in the long-wavelength region (green to red light), though residual absorption remains.

Table S2. Elemental content of Bi and V in Hexagon-$BiVO_4$ micromotors.

Element	Result
Bi	**65.12**
V	**15.48**

ICP-OES analysis was used to accurately determine the elemental composition of the Hexagon-$BiVO_4$ micromotor. The sample consisted of high-purity $BiVO_4$, with a Bi/V ratio of 1.03 ≈ 1, indicating that the Hexagon-$BiVO_4$ is of high purity and exhibits relatively stable photocatalytic activity**.**

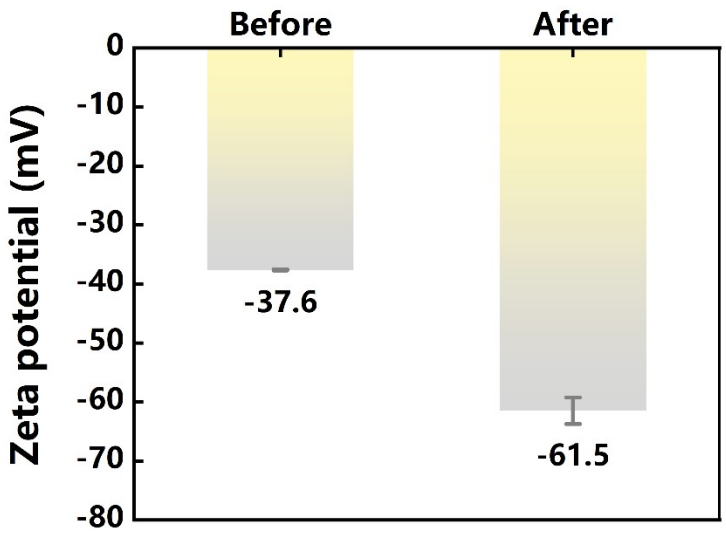

Figure S4. Comparison of the zeta potentials of Hexagon-$BiVO_4$ micromotors before and after the reaction.

The initial $BiVO_4$ micromotor suspension, with no light-induced reactions, had a zeta potential of -37.6 ± 0.1 mV, showing a clear negative charge. After driven by multi-wavelength light to move and complete interfacial reactions, the surface zeta potential changed to -61.5 mV, indicating an increased negative surface charge density. During the photocatalytic reaction, an asymmetric charge distribution forms that disappears afterward, although the surface chemistry of the micromotors is altered. These changes after the reaction cause the particles' average surface charge, indicated by zeta potential, to become more negative. The overall negative shift confirms that surface charges respond to light-induced carrier generation and supports the existence of an electrophoretic driving force due to asymmetric illumination.

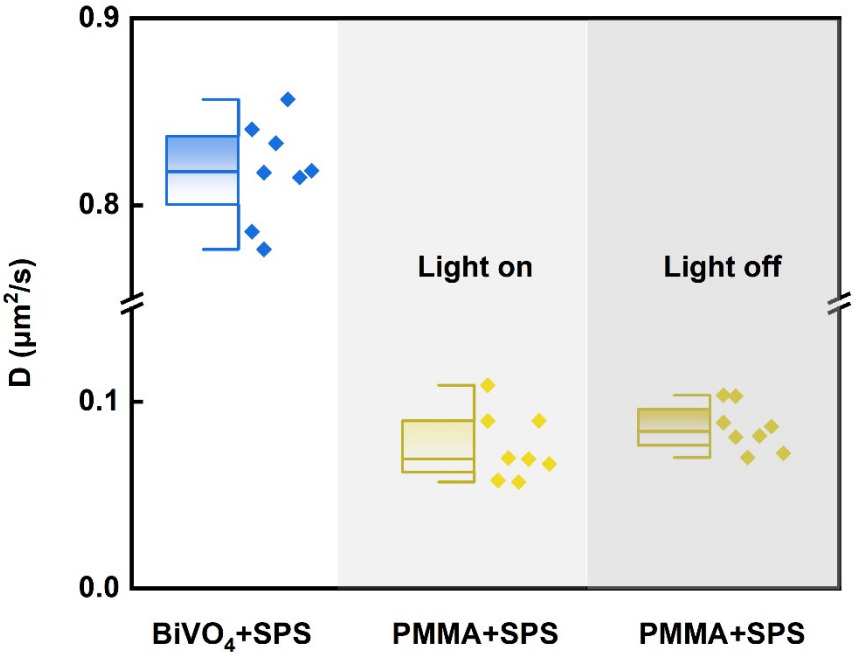

Figure S5. Diffusion coefficients of Hexagonal-$BiVO_4$ micromotors loaded with SPS under light-exposed conditions and of 5 μm PMMA microspheres loaded with SPS under both light-exposed and non-light-exposed conditions.

To verify the mobility of the SPS coating itself under illumination, a control experiment was conducted: SPS-loaded 5 μm PMMA microspheres were observed under both illuminated (455 nm, 96 mW/cm^2) and non-illuminated conditions. Their diffusion coefficients, derived from root-mean-square displacement data, were compared with those of SPS-loaded Hexagonal $BiVO_4$ micromotors under identical light conditions. The comparison results demonstrated that, regardless of illumination, the SPS-loaded PMMA microspheres showed only Brownian motion, with no sign of directed movement. This indicates that the SPS coating does not have an inherent self-propelling effect.

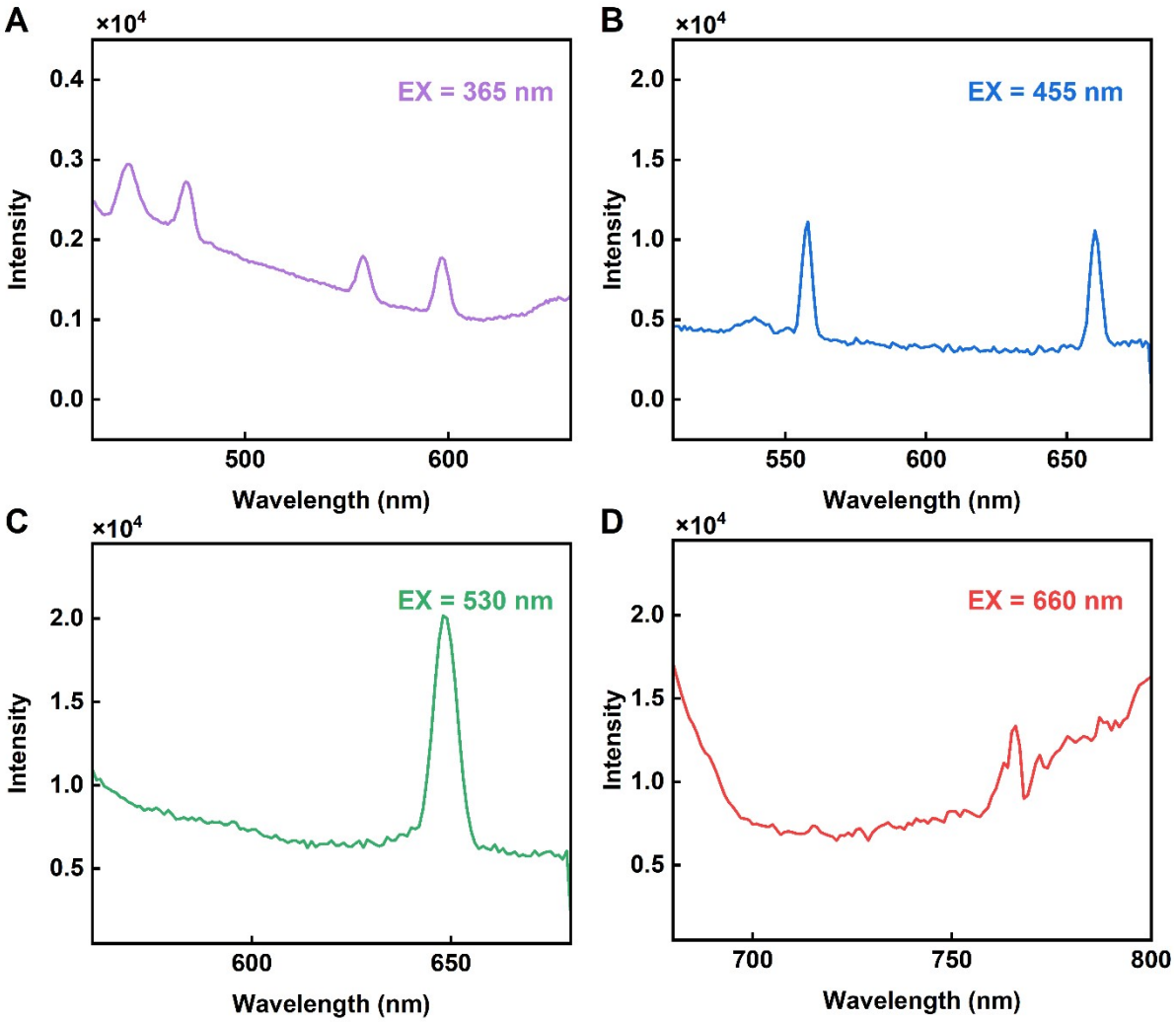

Figure S6. The photoluminescence spectra of Hexagon-$BiVO_4$ micromotors under different excitation wavelengths: (A) 365 nm**, (B)** 455 nm, **(C)** 530 nm, and **(D)** 660 nm.

Supplementary Note 3: Excitation wavelength (EX)

Combining the excitation wavelength, emission peak position, intensity, and shape, the photoluminescence spectrum of Hexagon-$BiVO_4$ micromotors is analyzed in terms of light response range, excitation-emission dependence, fluorescence characteristics, and application potential.

Under ultraviolet excitation (EX = 365 nm), the emission covers the visible spectrum, showing broad multi-peak emission (peaks near 470 nm and 580 nm), indicating multiple fluorescent centers or diverse energy transition pathways. Blue light excitation (EX = 455 nm) yields sharp, high-intensity dual emission peaks at around 560 nm and 650 nm, suggesting high energy conversion efficiency and potentially a high quantum yield. The excitation wavelength EX = 530 nm (green light) generates a strong, narrow single peak with an intensity peak approaching 2.0×10^4 at approximately 650 nm (red emission). This “green excitation → red emission” behavior ensures both tissue compatibility of the excitation light (green light causes minimal damage to biological tissues) and deep tissue penetration of the emission light (red light penetrates deeper than green light), making it highly suitable for bioimaging. Excitation at EX = 660 nm (red excitation) results in emission extending to ~800 nm (near-infrared, NIR), which is advantageous for biomedical applications (tissues exhibit weak absorption/scattering of NIR light, enabling penetration depths of several millimeters). This “red excitation → near-infrared emission” characteristic also suits scenarios such as deep tissue detection and optical communication. These demonstrate that Hexagon-$BiVO_4$ micromotors exhibit robust broadband light responsiveness, capable of being excited by multiple wavelengths, including ultraviolet (365 nm), blue (455 nm), green (530 nm), and red (660 nm) light. They generate fluorescence spanning the visible to near-infrared spectrum, enabling flexible control of "multi-wavelength excitation-multi-band emission" without

exhibiting coupling between excitation and emission wavelengths, making them adaptable to various optical manipulation scenarios. They hold potential applications in biomedical imaging, light-driven intelligent systems, and related fields.

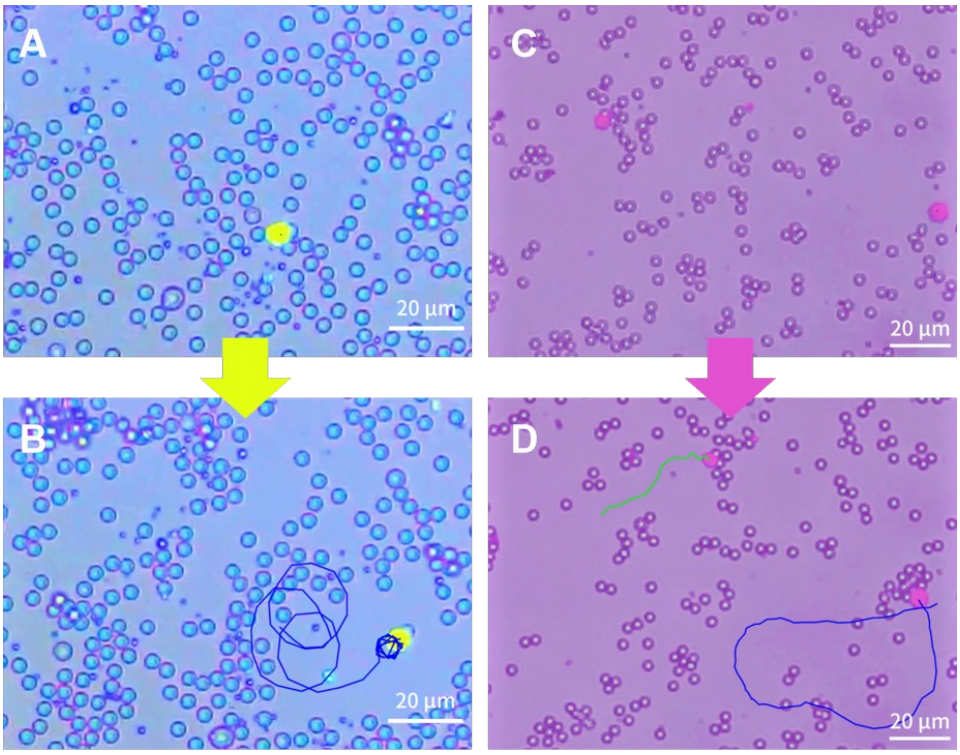

Figure S7. Motion behavior of Hexagon-$BiVO_4$ micromotors navigating PS or PMMA microsphere obstacles under optical control at different wavelengths (365 nm and 455 nm) (Movie S12-13). A. Distribution of PMMA particles before the movement of Hexagon-$BiVO_4$ micromotors under 455 nm blue light. **B.** Distribution of PMMA particles after the movement of Hexagon-$BiVO_4$ micromotors under 455 nm blue light. **C.** Distribution of PS particles before the movement of Hexagon-$BiVO_4$ micromotors under 365 nm UV light. **D.** Distribution of PS particles after the movement of Hexagon-$BiVO_4$ micromotors under 365 nm UV light.

Supplementary Note 4: Encountering obstacles

This experiment systematically investigated the motion characteristics of Hexagon-$BiVO_4$ micromotors in complex obstacle environments by precisely controlling wavelengths of the light sources (365 nm ultraviolet light and 455 nm blue light). Polystyrene (PS) microspheres and polymethyl methacrylate (PMMA) microspheres were selected as two typical obstacle models. The motion trajectories of Hexagon-$BiVO_4$ micromotors were comprehensively recorded, and the changes in obstacle distribution before and after the experiments were compared, providing critical data support for their environmental adaptability in practical applications.

Experimental observations revealed that when PS or PMMA microsphere obstacles were present along the preset motion path of the Hexagon-$BiVO_4$ micromotors, the mechanical resistance generated by these obstacles did not reach a critical value sufficient to block the micromotors' movement. Leveraging their unique propulsion mechanism, the micromotors could adjust their posture or dynamically regulate light-responsive forces to successfully bypass or traverse obstacle regions while maintaining stable speed and directional control. Further variable-controlled experiments demonstrated that neither changing the obstacle material (from hydrophobic PS microspheres to hydrophilic PMMA microspheres) nor switching the light-control wavelength (between 365 nm and 455 nm) caused significant motion deceleration or entrapment of the Hexagon-$BiVO_4$ micromotors. This fully proves their motion performance exhibits excellent interference resistance and environmental compatibility, unaffected by minor variations in obstacle material properties or light-control parameters.

Based on comparisons of particle distribution results, it was observed that during the traversal of obstacle regions, the strong motion of Hexagon-$BiVO_4$ micromotors generated fluid

disturbances or direct mechanical pushing, leading to noticeable spatial displacement of nearby PS/PMMA microspheres. Specifically, the particle density along the micromotors' motion trajectory decreased, while the density in surrounding areas comparatively increased. This phenomenon visually reflects that Hexagon-$BiVO_4$ micromotors not only possess outstanding obstacle-crossing abilities but also exhibit a certain degree of active obstacle-removing potential. This characteristic offers experimental evidence for their potential applications in complex microenvironments, such as biomedical fields (e.g., traversing extracellular matrix barriers during targeted drug delivery) and microfluidic chips (e.g., contaminant clearance in microchannels).

Table S3. Classification and Characteristics of Fluorescent Materials Commonly Used in Micro-Nano Fields.

Type of Fluorophore	Afterglow Duration	Key Advantages	Major Limitations
Organic Small-Molecule Dyes	20–30 s / several minutes (rapid decay under strong light)	High brightness, wide variety, easy labeling, small size	Susceptible to photobleaching, potential phototoxicity
Fluorescent Proteins (FPs)	0.1–30 s	Genetically encodable, high specificity, low toxicity	Large size, variable brightness, moderate photostability
Quantum Dots (QDs)	5–10 h (in buffer) / 1–3 h (in vivo)	Extremely high brightness, exceptional stability, tunable emission	Potential heavy metal toxicity, large size, blinking behavior
Carbon Nanodots (CDs)	Several hours (under continuous illumination)	Low toxicity, excellent biocompatibility, simple synthesis	Generally lower brightness and color purity compared to top-tier dyes and QDs
Upconversion Nanoparticles (UCNPs)	20–40 h (in vitro) / 2–5 h (in vivo)	No photobleaching, NIR excitation, deep tissue penetration, low toxicity	Relatively low brightness (quantum yield) requires high-power laser excitation.

Supplementary Note 5: Fluorescent Marking Technology Comparison

In biomedical research on micromotors (MNRs), fluorescence imaging technology serves as a core method for achieving dynamic tracking, evaluating targeting efficiency, and monitoring in vivo behavior. Currently, fluorescence labeling of MNRs predominantly relies on exogenous fluorophores, which mainly fall into five categories: small-molecule organic dyes, fluorescent proteins, quantum dots (QDs), carbon nanodots (CNDs), and upconversion nanoparticles (UCNPs). Their main performance parameters (e.g., afterglow duration), core advantages, and inherent limitations are described in Table S2.

However, the application of these fluorophores faces common technical challenges: accurately attaching them to MNRs requires additional steps, such as physical adsorption, polymer encapsulation, covalent conjugation, and surface grafting. This process inevitably exerts negative regulatory effects on the native structure and motion performance of MNRs—physical loading may introduce size redundancy or change surface energy, resulting in hydrodynamic imbalance. At the same time, chemical conjugation can consume active surface sites on MNRs, interfering with the functionality of driving units (e.g., magnetic-responsive coatings or chemical fuel reaction sites). Ultimately, these problems lead to lower propulsion efficiency and diminished targeting accuracy.

The Hexagon-$BiVO_4$ micromotors in this study have a key feature: inherent autofluorescence, which allows for effective imaging without needing to load external fluorophores. When compared to traditional labeling methods, the fluorescence ability of Hexagon-$BiVO_4$ micromotors offers three primary benefits:

1. The fluorescence property originates from the inherent photophysical response of the material, preventing motion interference caused by secondary processing and achieving

synergistic "imaging-motion" functionality.

2. Upon light excitation, the autofluorescence lasts for several hours, with an afterglow duration greatly exceeding that of existing fluorophores, supporting long-term dynamic tracking.

3. The autofluorescence process does not release toxic substances, significantly improving biocompatibility and establishing a vital basis for in vivo experiments and future clinical applications.

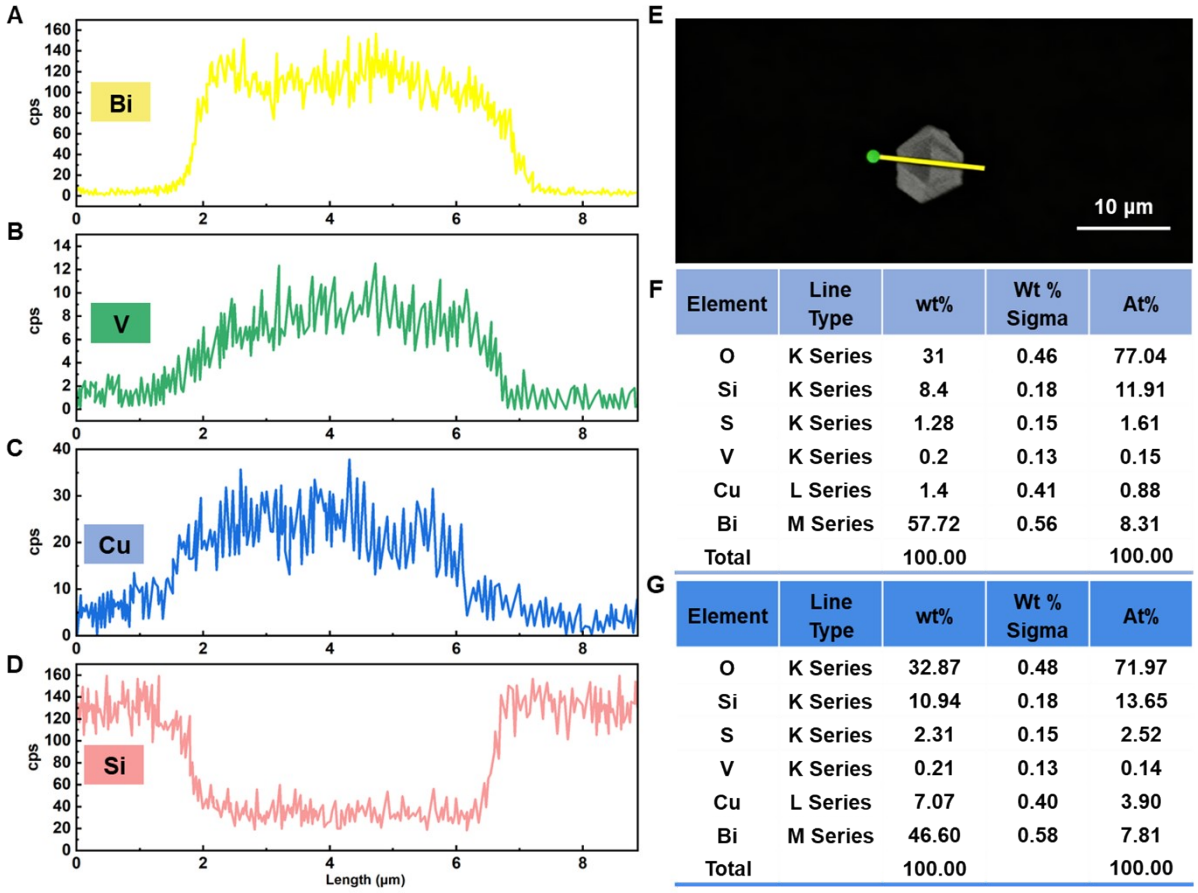

F

Element	Line Type	wt%	Wt % Sigma	At%
O	K Series	31	0.46	77.04
Si	K Series	8.4	0.18	11.91
S	K Series	1.28	0.15	1.61
V	K Series	0.2	0.13	0.15
Cu	L Series	1.4	0.41	0.88
Bi	M Series	57.72	0.56	8.31
Total		100.00		100.00

G

Element	Line Type	wt%	Wt % Sigma	At%
O	K Series	32.87	0.48	71.97
Si	K Series	10.94	0.18	13.65
S	K Series	2.31	0.15	2.52
V	K Series	0.21	0.13	0.14
Cu	L Series	7.07	0.40	3.90
Bi	M Series	46.60	0.58	7.81
Total		100.00		100.00

Figure S8. Hexagon-$BiVO_4$ micromotors in river water containing exogenously added $CuSO_4$. A-D. Elemental distributions of Bi, V, Cu, and Si from line scan data on a Hexagon-$BiVO_4$ micromotor after motion in $CuSO_4$-amended river water. **E.** Line scan position on the Hexagon-$BiVO_4$ micromotor. **F.** Line-scan elemental composition data collected after the micromotors were activated by light. **G.** Line-scan elemental composition data collected from the micromotors without light activation (same time as Figure S7F).

Supplementary Note 6: Validation Experiment of Copper Ion-Added River Water Solution

This study aims to evaluate the dynamic remediation capability of Hexagon-$BiVO_4$ micromotors toward heavy metal ions in aqueous systems, using Cu^{2+} as a model pollutant. Hexagon-$BiVO_4$ micromotors were introduced into a $CuSO_4$ solution of specified concentration and allowed to react under mercury-lamp irradiation. Systematic characterization of the post-reaction micromotor surfaces was performed via EDS mapping and point analysis. Distinct characteristic signals of copper were clearly detected on the micromotor surfaces, with spatial distribution highly coincident with the deposition regions. Furthermore, by distinguishing the copper ion enrichment results based on whether the motion was triggered by light, the comparison of elemental concentrations in Figures S6F and Figures S6G shows that it was the motion of micromotors that induced the adsorption of copper ions. These results directly confirm the specific adsorption and enrichment of copper ions on the Hexagon-$BiVO_4$ micromotor surfaces. Collectively, the findings provide robust evidence that Hexagon-$BiVO_4$ micromotors can effectively adsorb and remove copper ions from aqueous solutions, supporting their potential as a controllable, easily retrievable novel adsorbent for heavy metal remediation.

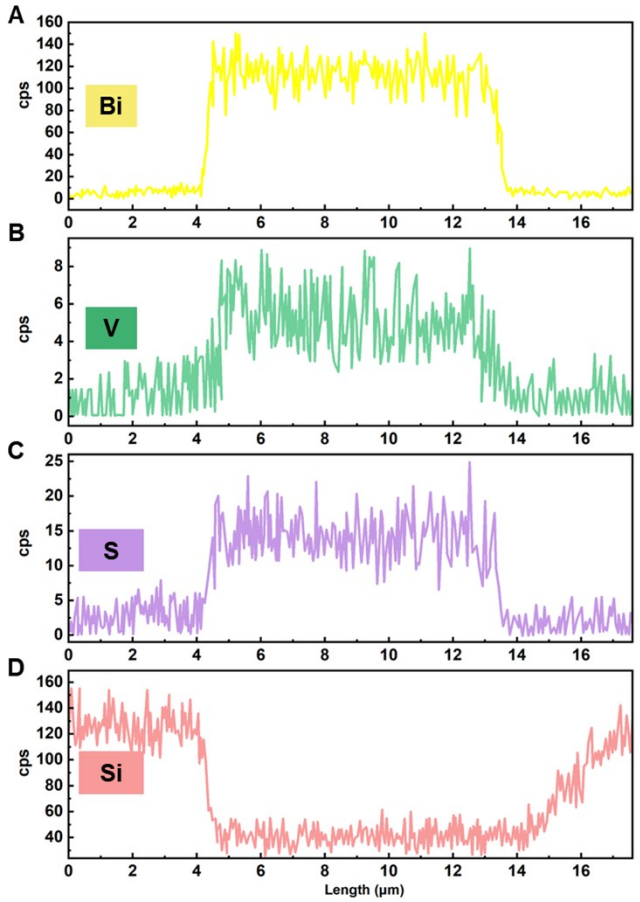

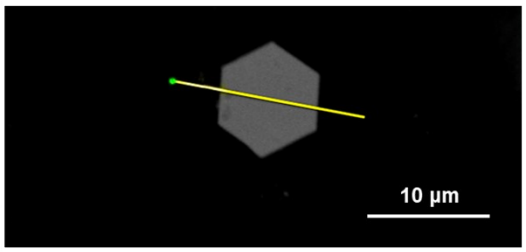

F

Element	Line Type	wt%	Wt % Sigma	At%
C	K Series	10.87	0.57	25.30
N	K Series	0.34	0.61	0.68
O	K Series	30.00	0.50	52.41
Si	K Series	15.31	0.24	15.24
S	K Series	0.26	0.11	0.23
Cl	K Series	0.45	0.12	0.36
V	K Series	0.14	0.11	0.08
Bi	M Series	42.62	0.66	5.70
Total		100.00		100.00

Figure S9. Hexagon-$BiVO_4$ micromotors in river water containing exogenously added methylene blue. A-D. Elemental distributions of Bi, V, S and Si from line scan data on a Hexagon-$BiVO_4$ micromotor after motion in methylene blue-amended river water. **E.** Line scan position on the Hexagon-$BiVO_4$ micromotor. **F.** Elemental content from the corresponding line scan data.

Supplementary Note 7: Verification Experiment of River Water Solution with Methylene Blue Addition

To elucidate the synergistic removal mechanism of Hexagon-$BiVO_4$ micromotors for organic pollutants, this study designed and conducted a photocatalytic degradation experiment using methylene blue (MB) as a model dye contaminant. Hexagon-$BiVO_4$ micromotors at a defined concentration were dispersed in a river water solution containing 5 mg L^{-1} of MB and reacted under mercury-lamp irradiation. Comparison of solution decolorization times revealed that the Hexagon-$BiVO_4$ micromotor group decolorized significantly faster than the blank control (without motors) and the group containing only static catalytic material, showing approximately 10% greater degradation efficiency. To investigate the underlying mechanism, the reacted Hexagon-$BiVO_4$ micromotors were subjected to detailed surface analysis. SEM images showed no change in surface morphology, while EDS analysis detected signals of characteristic MB elements, such as nitrogen and sulfur, on the motor surfaces. These results directly demonstrate that, during the photocatalytic degradation of MB, Hexagon-BiVO4 micromotors also effectively adsorb and enrich MB molecules or degradation intermediates on their surfaces. By combining degradation kinetics with solid-state characterization, this work confirms that Hexagon-$BiVO_4$ micromotors possess dual functionality—adsorptive capture and photocatalytic decomposition—toward methylene blue, providing key evidence for their application as an efficient, integrated platform for water remediation.

Movie S1.

Motion trajectory of the Hexagon-$BiVO_4$ micromotor under illumination at 365 nm.

Movie S2.

Motion trajectory of the Hexagon-$BiVO_4$ micromotor under illumination at 455 nm.

Movie S3.

Motion trajectory of the Hexagon-$BiVO_4$ micromotor under illumination at 530 nm.

Movie S4.

Motion trajectory of the Hexagon-$BiVO_4$ micromotor under illumination at 660 nm.

Movie S5.

Comparison of the trajectory of the Hexagon-$BiVO_4$ micromotor during light switching "off" and "on" under 365 nm.

Movie S6.

Comparison of the trajectory of the Hexagon-$BiVO_4$ micromotor during light switching "off" and "on" under 455 nm.

Movie S7.

Comparison of the trajectory of the Hexagon-$BiVO_4$ micromotor during light switching "off" and "on" under 530 nm.

Movie S8.

Comparison of the trajectory of the Hexagon-$BiVO_4$ micromotor during light switching “off” and “on” under 660 nm.

Movie S9.

Boosted motion performance of the Hexagon-$BiVO_4$ micromotor actuated by 455 nm light in a 7.5 mmol/L urea solution.

Movie S10.

Boosted motion performance of the Hexagon-$BiVO_4$ micromotor actuated by 455 nm light in a 10 mmol/L glucose solution.

Movie S11.

Detection of fluorescent Hexagon-$BiVO_4$ micromotor under 455 nm irradiation was observed with a 4× objective.

Movie S12.

Motion behavior of Hexagon-$BiVO_4$ micromotors through 2 μm PS obstacles under 365 nm.

Movie S13.

Motion behavior of Hexagon-$BiVO_4$ micromotor through 2 μm PMMA obstacles under 455 nm.

Movie S14.

Observation of the trajectory of fluorescent Hexagon-$BiVO_4$ micromotors in river water under mercury lamp illumination

Reference

1 L. Huang, Z. Duan, Y. Song, Q. Li, and L. Chen, *ACS Appl. Nano Mater.*, 2021, **4**, 3576–3585.

2 Z. Chen, N. Mi, L. Huang, W. Wang, C. Li, Y. Teng, and C. Gu, *Sci. Total Environ.,* 2022, **808**, 152083.

3 S. Zhang, X. Jiang, Y. Jiang, C. Jiang, and X. Yao, *Ind. Eng. Chem. Res.*, 2023, **62**, 1277–1285.

4 D. Philo, S. Luo, C. He, Q. Wang, F. Ichihara, L. Jia, M. Oshikiri, H. Pang, Y. Wang, S. Li, G. Yang, X. Ren, H. Lin and J. Ye, *Adv. Funct. Mater.*, 2022, **2**, 955-964.

5 T. Ahmed, H. Zhang, Y.-Y. Gao, H. Xu and Y. Zhang, *Mater. Res. Bull.*, 2018, **99**, 298–305.

6 T. W. Kim and K.-S. Choi, *Science (1979).*, 2014, **343**, 990–994.

7 L. Fu, W. Lian, Y. Lin, W. Fang, R. Xv and X. Shang, *ACS Appl. Energy Mater.*, 2023, **6**, 10116–10127.

8 X. Long, C. Shen, J. Wei, Q. Gao, and X. Zhao, *ACS Appl. Energy Mater.*, 2025, **8**, 1700–1708.

9 M. G. Guardiano, L. K. Ribeiro, I. M. D. Gonzaga, and L. H. Mascaro, *ACS Appl. Nano Mater.*, 2024, **7**, 19569–19578.

10 M. Nodehi, M. Zirak, O. Reiser, H. Alehdaghi, M. Kazemi, M.-S. Koshki, N. Rabiee

and M. Baghayeri, *ACS Appl. Eng. Mater.,* 2024, **2**, 955–964.

11 R. Dell'Oro, M. Sansotera, C. L. Bianchi and L. Magagnin, *ACS Omega*, 2023, **8**, 20332–20341.

12 B. Peng, X. Zhao, C. Li, D. Zhang, N. Zhou, Y. Zhou, S. Ding, Z. Wu, and Y. Xiong, *ACS Appl. Nano Mater.*, 2025, **8**, 18174–18182.

13 K. Villa, F. Novotný, J. Zelenka, M. P. Browne, T. Ruml and M. Pumera, *ACS Nano*, 2019, **13**, 8135–8145.

14 G. M. Peleyeju, E. H. Umukoro, J. O. Babalola and O. A. Arotiba, *ACS Omega*, 2020, **5**, 4743–4750.

15 X. Mao and P. Chen, *Nat. Mater.*, 2022, **21**, 331–337.

16 T. Tachikawa, T. Ochi and Y. Kobori, *ACS Catal.*, 2016, **6**, 2250–2256.

17 K. Villa, F. Novotný, J. Zelenka, M. P. Browne, T. Ruml and M. Pumera, *ACS Nano*, 2019, **13**, 8135–8145.

18 J. M. Gonçalves, L. N. Córdoba Urresti, Y. Chen and K. Villa, *Chem. Commun.,* 2025, **61**, 11834–11837.

19 V. D. Lovasz, J. M. Gonçalves, G. A. Vinnacombe-Willson, L. M. Liz-Marzán and K. Villa, *Research*, 2026, **9**, 1110.

20 R. Li, F. Zhang, D. Wang, J. Yang, M. Li, J. Zhu, X. Zhou, H. Han and C. Li, *Nat. Commun.*, 2013, **4**, 1432.